East European Journal of Physics. 3. 44–53 (2026)
DOI: 10.26565/2312-4334-2026-3-04 ISSN 2312-4334

ON THE NUCLEAR STRUCTURE AND STELLAR WEAK RATES OF NEUTRON-RICH $^{104-116}$Rh ISOTOPES

Abdul Kabir[1*], **Jameel-Un Nabi**[2], **Rahat Badshah**[1], **Ayesha Anjum**[2]
[1]*Department of Space Science, Institute of Space Technology, Islamabad, 44000, Pakistan*
[2]*Department of Physics, University of Wah, Wah cantt, 47040, Pakistan*
[*]*Corresponding Author e-mail: kabirkhanak1@gmail.com*
Received April 3, 2026; revised June 22, 2026; accepted July 10, 2026

The nuclear ground state and beta decay properties of neutron-rich odd-odd and odd-A $^{104-116}$Rh isotopes are studied by utilizing the relativistic mean-field (RMF) and proton-neutron quasi-particle random phase approximation (pn-QRPA) models. Potential energy surfaces and potential energy curves are examined to investigate the nuclear deformations, nuclear stability, and shape phase transitions. The Gamow-Teller (GT) strength distributions and β-decay properties are obtained based on a deformed pn-QRPA framework. The computed half-lives and log ft values are in good agreement with existing experimental data, supporting the utilization of nuclear models. Additionally, stellar weak interaction rates are calculated as a function of density and temperature, emphasizing their influence on nucleosynthesis in astrophysical environments. For neutron-rich Rh isotopes, the results provide useful nuclear structural data and reliable inputs for the r-process modeling.

Keywords: *pn-QRPA; Nuclear ground state properties; Stellar weak rates; Potential energy surfaces; Log ft*

1. INTRODUCTION

The GT strength of atomic nuclei is extensively investigated and applied in nuclear and astrophysical research. It makes a substantial contribution to nuclear spectroscopy. Accurate modeling and a more comprehensive understanding of foundational nuclear processes depend on precise measurements and underlying theories related to the low-energy nuclear structure, including the GT strengths, half-lives, and stellar weak rates. The study of the available nuclear ground state properties remains a fundamental pillar in nuclear astrophysics today. It provides the information needed to comprehend the forces that dominate many-body nucleonic systems [1].

The neutron-rich nuclei are mostly unstable and have unique properties such as structural evolution, different shell closures, altered binding energies, and distinct β decay patterns compared to stable isotopes. Neutron-rich nuclei primarily decay via the β^- mechanism, where a neutron transforms into a proton by emitting an electron. Before decay, the nucleus is far from the stability line. The decay changes the element (e.g., Rh decays to Pd) and moves the nucleus closer to the line of stability, balancing the neutron-proton ratio. Particularly, the β^- decay properties, including the half-lives and GT strength, provide essential information about the stellar weak interaction rates that play an important role in nucleosynthesis processes [2]. The beta decay properties are calculated using the pn-QRPA model [3–5]. The neutron-rich nuclei in the mass range $A \sim$ 110-120 have attracted considerable attention from both theoretical and experimental studies as they show rapid variation observed in their ground-state structure and low-lying excited states [6, 7]. The information about the nuclear structure is carried by the GT strength distribution. It largely depends on the ground-state deformation of the parent nuclei [8]. Neutron-rich nuclei in the mass range $A \sim$ 104–113 exhibit rapid structural evolution due to deformation, pairing correlations, and shell effects. A large number of nuclei in this mass region are located far from the valley of β stability and are therefore not accessible to experimental investigations. Consequently, their properties must be studied using theoretical approaches. It is estimated that nearly 6000 nuclei exist between the valley of β stability and the neutron drip line. This specific location makes Rh isotopes ideal for studying the conflict between the effects of the spherical shell and the initial phases of collective deformation [9–13]. Nuclear density functional theory provides the theoretical foundation for the analysis of nuclear ground-state properties, especially nuclear deformation and nuclear shape transitions from oblate to prolate shapes. In the present analysis, we employed the RMF model with the density-dependent meson (DD-ME2) interaction to extract the nuclear deformation of the nuclei under investigation. The pn-QRPA model has been used for spectroscopic investigations including log ft values, half-lives and stellar weak rates [14] of Rh nuclei. Both RMF and pn-QRPA models are widely employed for the investigation of nuclear structure and β decay properties. The RMF framework is based on a small number of parameters optimized using nuclear matter properties and experimental data of stable nuclei located near the valley of β stability [15].

The present work is structured as follows. Section 2 provides a brief explanation of the theoretical foundation. Section 3 discusses nuclear ground state parameters including decay half-lives, weak decay rates, predicted GT strength, and log ft values. The final portion contains our concluding observations.

Cite as: A. Kabir, J.-Un Nabi, R. Badshah, A. Anjum, East Eur. J. Phys. 3, 44 (2026), https://doi.org/10.26565/2312-4334-2026-3-04

2. THEORETICAL FRAMEWORKS

2.1. The RMF Model

The RMF model describes how nuclei exchange mesons and photons [16]. The incompressibility and surface attributes of nuclei were challenging for the initially proposed version of the RMF framework. In order to accomplish this, a nonlinear framework of RMF was developed [17]. Following the introduction of further model versions, such as DD-ME2 and DD-PC1, the concept was referred to as covariant density functional theory (CDFT) [18, 19]. In the present investigation, we used the DD-ME2 version of the model. Conventional quantum hydrodynamics uses Dirac fermions coupled to meson exchange as an effective Lagrangian to describe a nuclide [20, 21]. The RMF approach defines the simplest set of meson fields for determining the bulk and single-particle nuclear parameters, employing the isoscalar scalar (σ), isoscalar vector (ω), and isovector vector (ρ) meson fields [7, 22]. The Lagrangian density can be expressed as follows:

$$\begin{aligned} L = \bar{\psi}[\gamma_\mu(i\partial^\mu - \Gamma_\omega\omega^\mu - \Gamma_\rho\vec{\tau}\cdot\vec{\rho}_\mu) - (M - \Gamma_\sigma\sigma) - e\gamma^\mu A_\mu\frac{1-\tau_3}{2}]\psi + \frac{1}{2}(\partial^\mu\sigma\partial_\mu\sigma - m_\sigma^2\sigma^2) \\ -\frac{1}{4}\Omega^{\mu\nu}\Omega_{\mu\nu} + \frac{1}{2}m_\omega^2\omega^\mu\omega_\mu - \frac{1}{4}\vec{R}^{\mu\nu}\cdot\vec{R}_{\mu\nu} + \frac{1}{2}m_\rho^2\vec{\rho}^\mu\cdot\vec{\rho}_\mu - \frac{1}{4}F^{\mu\nu}F_{\mu\nu}, \end{aligned} \tag{1}$$

where Γ_σ, Γ_ω, and Γ_ρ are the coupling constants and depend on the (nucleon) density and are described as

$$\Gamma_i(\rho) = \Gamma_i(\rho_{\text{sat}})f_i(x), \tag{2}$$

where $i = \sigma, \omega$ and ρ mesons. $f(x)$ is a function of $x = \rho_b/\rho_{\text{sat}}$, where ρ_b is the baryon density and ρ_{sat} is the baryon density at saturation in symmetric nuclear matter. For σ or ω meson, the respective $f(x)$ is

$$f_j(x) = a_j\frac{1+b_j(x+d_j)^2}{1+c_j(x+d_j)^2}, \quad \text{where } j = \sigma, \omega, \tag{2}$$

where for the ρ meson,

$$f_\rho(x) = e^{(-a_\rho(x-1))}. \tag{3}$$

Modifying the Lagrangian with reference to $\bar{\psi}$ yields the single-nucleon Dirac equation with nucleon self-energies [23, 24]. We utilize the Dirac-Hartree-Bogoliubov (DIRHB) code [23] to generate the PEC and PES of $^{104-116}$Rh as a function of β_2 and γ, using DD-ME2 [25] interactions. The β_2 and γ are calculated below:

$$\beta_2 = \sqrt{a_{20}^2 + 2a_{22}^2} \ \text{ and } \ \gamma = \arctan(\sqrt{2}\,\frac{\mathrm{a}_{22}}{\mathrm{a}_{20}}), \tag{4}$$

where a_{20} and a_{22} are the deformation parameters computed via Ref. [23]. Quadrupole moment constraints were used in RMF calculations to achieve these calculations. The pairing correlations, which are assumed to be essential for open-shell nuclei, were investigated using the Bardeen-Cooper-Schrieffer (BCS) method. Furthermore, the ground state variables stated above were determined utilizing the constant G approximation [26].

2.2. The pn-QRPA Model

The stellar weak rates are described within the framework of the pn-QRPA model. The Hamiltonian of the pn-QRPA model is structured as follows:

$$H^{QRPA} = H^{sp} + V^{pair} + V_{GT}^{pp} + V_{GT}^{ph} \tag{5}$$

where H^{sp}, V^{pair}, V_{GT}^{pp} and V_{GT}^{ph} are the single-particle Hamiltonians, the pairing potential, the particle-particle, and the particle-hole strength, respectively. The wave functions and energy of a single particle were assessed using the Nilsson approach [27]. The Nilsson potential variables have been selected based on Ref. [28]. The Q-energies were analyzed utilizing the mass excess from Ref. [29] and β_2 from the RMF Ref. [30]. These assessments were conducted independently for protons (neutrons), employing a constant pairing force of strength G (G_n for neutrons and G_p for protons):

$$V_{pair} = -G\sum_{jkj'k'}(-1)^{l+j-k}s_{jk}^\dagger s_{j-k}^\dagger \times (-1)^{l'+j'-k'}s_{j'-k'}s_{j'k'},$$

Only positive numbers k and k' are to be summed over. The nucleon's spherical basis ($s_{jk}, s_{jk}^\dagger$) is transformed into a deformed basis ($d_{k\alpha}, d_{k\alpha}^\dagger$) using:

$$d_{k\alpha}^\dagger = \Sigma_j D_j^{k\alpha}s_{jk}^\dagger, \tag{6}$$

The Hamiltonian was diagonalized via an additional quantum number α to create $D^{k\alpha}$. The Bogoliubov transformation was applied to obtain the quasi-particle basis ($q_{k\alpha}^\dagger, q_{k\alpha}$).

$$q_{k\alpha}^\dagger = u_{k\alpha}d_{k\alpha}^\dagger - v_{k\alpha}d_{\bar{k}\alpha}, \tag{7}$$

$$q^{\dagger}_{\bar{k}\alpha} = u_{k\alpha} d^{\dagger}_{\bar{k}\alpha} + v_{k\alpha} d_{k\alpha}, \tag{8}$$

$\bar{k}$ denoted k's time-reversed state. The occupancy was determined using the BCS equations, with the basis $v^2_{k\alpha} + u^2_{k\alpha}$ = 1. The random phase approximation (RPA) framework is used to handle the residual interaction introduced in the Hamiltonian that establishes ground-state correlation. The pn-QRPA phonon creation operators are as follows:

$$A^{\dagger}_{\omega}(\mu) = \sum_{pn} [X^{pn}_{\omega}(\mu) q^{\dagger}_{p} q^{\dagger}_{\overline{n}} - Y^{pn}_{\omega}(\mu) q_n q_{\overline{p}}], \tag{9}$$

X_ω and Y_ω are the phonon amplitudes, while n and p are the quasi-particle states. The sum p-n pairings satisfy $\mu = k_n - k_p$=(1, 0, -1) and $\pi_n \cdot \pi_p$=1. The RPA expresses the eigenvalue as ω, which is the excitation energy. The particle-particle interaction (κ) and particle-hole interaction (χ) are the GT forces that are considered to be residual forces within the framework of pn-QRPA. The basis for the particle-particle forces is expressed as:

$$V^{pp}_{GT} = -2\kappa \sum_{\mu=-1}^{1} (-1)^{\mu} O^{\dagger}_{\mu} O_{-\mu}, \tag{10}$$

with

$$O^{\dagger}_{\mu} = \sum_{j_p k_p j_n k_n} < j_n k_n \mid (t_{\pm}\sigma_{\mu})^{\dagger} \mid j_p k_p > \times (-1)^{l_n + j_n - k_n} s^{\dagger}_{j_p k_p} s^{\dagger}_{j_n - k_n}.$$

Furthermore, in order to examine the χ interaction, we employed:

$$V^{ph}_{GT} = +2\chi \sum_{\mu=-1}^{1} (-1)^{\mu} U_{\mu} U^{\dagger}_{-\mu}, \tag{11}$$

with

$$U_{\mu} = \sum_{j_p k_p j_n k_n} < j_p k_p \mid t_{\pm}\ \sigma_{\mu} \mid j_n k_n > s^{\dagger}_{j_p k_p} s_{j_n k_n}. \tag{12}$$

Incorporating the residual interaction is essential for accurately reproducing reported GT strength and has a significant effect on the computed GT strength. The GT matrix element has been computed using

$$B_{GT}(\omega) = |\langle \omega, \mu || \tau_{-} \sigma_{\mu} || QRPA \rangle|^2. \tag{13}$$

The partial half-lives ($t_{1/2}$) were analyzed using the following formula.

$$t_{1/2} = \frac{\kappa}{(g_A/g_V)^2 f(A,Z,E) B_{GT}(\omega) + f(A,Z,E) B_F(\omega)}, \tag{14}$$

g_A/g_V is the ratio of axial and vector coupling constants, and κ = 6143 s [27]. $f(A,Z,E)$ is the phase space integral. B_F and B_{GT} are the Fermi and GT matrix elements, respectively. The beta-decay half-lives are computed as

$$T_{1/2} = \left(\sum_{0 \leq \omega \leq Q} (\frac{1}{t_{1/2}}) \right)^{-1}. \tag{15}$$

For additional analysis of Eq. (5), see [28, 29]. Taking into account the above relation, we obtain the relation for the *ft* as follows:

$$ft = \frac{\kappa}{(g_A/g_V)^2 B_{GT} + B_f} \tag{16}$$

The stellar weak rates were calculated from the initial state i to the final state f by utilizing

$$\lambda^{\beta^-/PC}_{if} = \ln 2 \frac{f^{\beta^-/PC}_{if}(\rho, T, E_f)}{(ft)_{if}}. \tag{17}$$

The $(ft)_{if}$ is represented as:

$$ft_{if} = (g_A/g_V)^2 B^{if}_{GT} + B^{if}_{F}, \tag{18}$$

$$B^{if}_{GT} = \frac{1}{2\mathcal{J}+1} \langle \psi_f \parallel \sum_k \tau^k_{-} \overrightarrow{\sigma}^k \parallel \psi_i \rangle|^2, \tag{19}$$

$$B_F^{if} = \frac{1}{2\mathcal{J}+1}\langle\psi_f \parallel \sum_k \tau_-^k \parallel \psi_i\rangle|^2. \tag{20}$$

where $\mathcal{J}$ is the angular momentum of the initial state. The analysis of nuclear matrix elements and the creation of low-lying excited states in our present investigation may be mentioned in [29]. The phase space integrals $f_{if}^{\beta^-/PC}$ are defined to be dimensionless and depend on certain stellar variables, including the stellar density and stellar temperature. Phase space integrals are expressed as:

$$f_{if}^{\beta^-} = \int_1^{E_\beta} E_k\sqrt{E_k^2-1}(E_\beta - E_k)^2 F(Z,E_k)(1-G_-)dE_k. \tag{21}$$

The f_{if}^{PC} for positron capture was evaluated using:

$$f_{if}^{PC} = \int_{E_l}^{\infty} E_k\sqrt{E_k^2-1}(E_\beta + E_k)^2 F(-Z,E_k)G_+ dE_k, \tag{22}$$

where E_k and E_β are the electron kinetic energy and the threshold energy during capture or emission. Energies are stated in units of the electron rest mass ($m_e c^2$). We further adopted natural units ($\hbar = c = m_e = 1$), where m_e is the electron rest mass. $F(+Z, E_k)$ is calculated using the approach described in Ref. [30]. We determined the β decay kinematics with:

$$E_\beta = m_p - m_d + E_p - E_d, \tag{23}$$

E_p, m_p and m_d, E_d denotes the parent and daughter nuclei's respective excitation energies and masses. The functions $G_\mp$ mentioned in equation (21) are defined as:

$$G_- = \left[\exp\left(\frac{E_k - E_f}{k_b T}\right) + 1\right]^{-1}, \tag{24}$$

$$G_+ = \left[\exp\left(\frac{E_k + 2 - E_f}{k_b T}\right) + 1\right]^{-1}, \tag{25}$$

where k_b refers to the Boltzmann constant and E_f is the Fermi energy of the electron. The number density of protons and neutrons was calculated by

$$\rho Y_e N_A = \frac{1}{\pi^2}\left(\frac{m_e c}{h}\right)^3 \int_0^\infty (G_- - G_+)p^2 dp, \tag{26}$$

Y_e and N_A represent the electron-proton ratio and Avogadro number, respectively. p represents the momentum of leptons. Stellar rates are determined with:

$$\lambda^{\beta^-/PC} = \sum_{if} P_m \lambda_{if}^{\beta^-/PC}, \tag{27}$$

where P_m represents the parent nucleus occupation probability. We summed the initial and final states until our computed rates reached the desired level of convergence.

3. RESULTS AND DISCUSSION

We conducted a systematic analysis of the nuclear deformation for $^{104-116}$Rh based on the potential energy curves (PEC's) and potential energy surfaces (PES's), utilizing the RMF model. For this purpose, we computed the total binding energy of the nuclei by constraining the β_2 and γ via the RMF model with the DD-ME2 interaction. The PEC and PES allow us to accurately demonstrate the phase shape transition of a particular isotope favors a prolate, oblate or spherical shape. In order to obtain the PEC, we set a zero reference point at the minimum energy. The difference between the binding energy at the particular β_2 and lowest binding energy, is plotted against β_2. In the mean-field model, a reliable convergence can be achieved by considering as many shells of harmonic oscillators of Fermion (N_F) and boson (N_B). However, the computation time increases significantly as the N_F, and N_B increases. We calculate the ground-state observable keeping $N_F = 12$ and $N_B = 12$. Increasing the nucleon number causes a transition in the shape of the nuclei, especially around magic numbers or mid shells. It is evident from PEC's analysis as displayed in Fig. 1 that nuclei possessing the neutron numbers $N = 59$ and 60 have a prolate shape, while $N = 62, 63, 64, 65, 67, 68, 69$, and 71 exhibit an oblate shape in the ground state. However, the $N = 60$ and 61 isotopes have substantial shape coexistence. ^{106}Rh has two local minima at β_2 = -0.275 on Ex = 0.0 MeV and at β_2 = 0.2 on Ex = 0.107 MeV via the DD-ME2 interaction. To generate the PES for the listed nuclei, considerations were given to both β_2 and γ deformations. Quadrupole shape deformations can be expressed in terms of polar coordinates β_2 and γ. The prolate and oblate shapes are related to $\gamma = 0°$, and $\gamma = 60°$, respectively. On the other hand, degrees of freedom are associated with the triaxial form ($0 \le \gamma \le 60$). In this particular analysis, the restrictions were execute to the PES and deformations in the β_2-γ plane ($0 \le \gamma \le 60$). The minima spread in the γ direction indicates a tendency of gamma softness. From the PES's analysis as mentioned in Fig. 2, ^{104}Rh has a prolate shape in its ground state, while ^{105}Rh, ^{106}Rh, ^{107}Rh, and ^{108}Rh have triaxial shapes. These isotopes have both the prolate

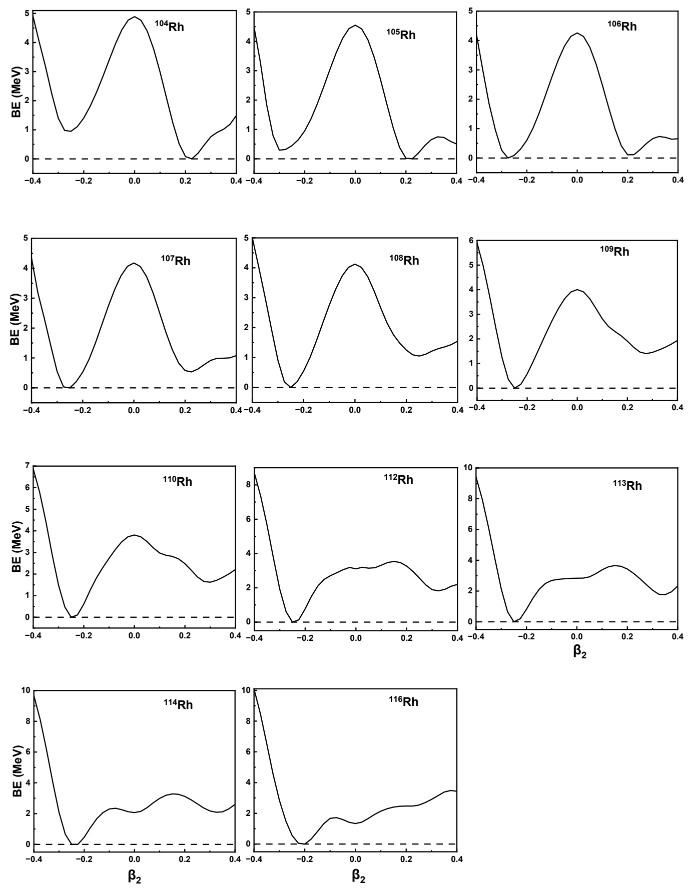

Figure 1. Calculated PECs for Rh isotopes using the RMF with DD-ME2 interaction.

and oblate minima on the PEC plot against β_2. Compared to the prolate energy minima, the oblate energy minima for ^{105}Rh, ^{106}Rh, ^{107}Rh, and ^{108}Rh are shallower. As a result, the ground state of these nuclei is more likely in a prolate shape. Furthermore, the present investigation predicts the coexistence with minimal energy difference in $^{104-116}$Rh isotopes. The present model-based extracted β_2, along with the existing β_2 from Ref. [32], is displayed in Table 1.

Table 1. The computed β_2 for $^{104-116}$Rh along with β_2 from Ref. [32].

Nuclei	[32]	This work
^{104}Rh	0.217	0.225
^{105}Rh	0.217	0.225
^{106}Rh	0.250	-0.275
^{107}Rh	0.250	-0.250
^{108}Rh	0.250	-0.250
^{109}Rh	0.262	-0.250
^{110}Rh	-0.248	-0.250
^{112}Rh	-0.248	-0.250
^{113}Rh	-0.248	-0.250
^{114}Rh	-0.258	-0.225
^{116}Rh	-0.258	0.250

In the subsequent part of our analysis, we employed the deformed pn-QRPA model to investigate the β decay properties, using the deformed pn-QRPA model. We used nuclear deformations from two different models, including the RMF model with DDME2 interaction and the FRDM model. Let us define our recipe: the beta decay properties investigated based on the deformation taken from the FRDM model is represented by pn-QRPA-FRDM, while the deformation taken from the RMF-DDME2-based interaction is represented by pn-QRPA-DDME2. Table 2 displayed the log ft values calculated using the pn-QRPA-FRDM and pn-QRPA-DDME2 along with experimental data [34] for ^{105}Rh, ^{113}Rh, and ^{114}Rh. The ratio between the computed and measured data is almost a factor of ≈ 1.5, which shows that the calculated log

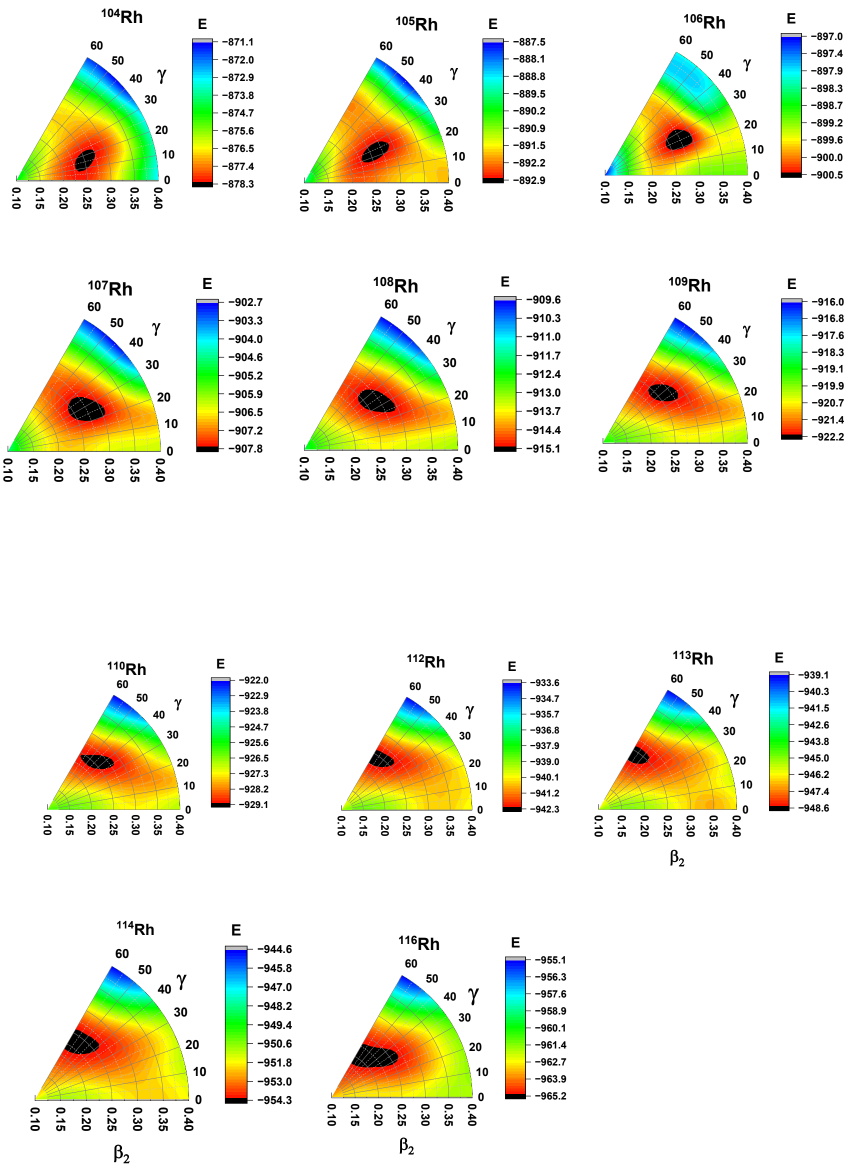

Figure 2. Calculated PES for Rh isotopes using the RMF with DD-ME2 interaction.

ft's are in good agreement with the experimental data. Figure 3 displays the comparison of the GT strength distributions, computed via the pn-QRPA-FRDM and pn-QRPA-DDME2 for ^{113}Rh as a function of excitation energy in the daughter nucleus. The experimental data exhibit a fragmented GT strength distribution, with most of the strength concentrated below 1.2 MeV. However, both pn-QRPA-FRDM and pn-QRPA-DDME2 calculations reproduce the general fragmentation pattern and the presence of low-lying GT transitions, which play a crucial role in determining the β-decay half-life. The calculations using both deformations predict relatively stronger GT strength at lower excitation energies. In contrast, model approximations, such as the omission of deformation effects in the daughter nuclei, may cause slight discrepancies between the computed and experimental results. Moreover, Fig. 3b represents the similar behavior for ^{114}Rh as is observed for ^{113}Rh, where the GT strength is distributed over a wide range of excitation energies with dominant contributions at low energies. The overall agreement between the calculated and experimental GT distributions demonstrates the reliability of the pn-QRPA-FRDM and pn-QRPA-DDME2 deformations as input parameters for the prediction of β-decay properties of neutron-rich Rh nuclei. Figure 4 compares our calculated half-lives for Rh nuclei with measured data [33]. Our predicted half-lives for Rh nuclei are about a factor of two greater or lower than the experimental data.

After examining the terrestrial half-lives, log ft values, and the GT strength distribution, considerations were given to the stellar weak rates, including the electron emission rates (λ^{β^-}) and positron capture rates (λ^{pc}) for the selected Rh nuclei. The stellar β-decay rates are important input parameters for simulating the late phases of massive stars. Other factors, e.g., magnetorotational effects [35], may also destabilize the stellar core. The stellar β-decay rates strongly depend

Table 2. Experimental [34] and calculated log ft values for neutron-rich Rh nuclei. Ratios are given to two decimal places.

Decay	E (keV)	log $ft_{\text{Exp.}}$	log $ft_{\text{pn-QRPA-FRDM}}$	log $ft_{\text{pn-QRPA-DDME2}}$	pn-QRPA-FRDM/Exp.	pn-QRPA-DDME2/Exp.
			^{105}Rh → ^{105}Pd			
$7/2^+ \rightarrow 5/2^+$	0	5.729	4.42	4.44	1.29	1.29
$7/2^+ \rightarrow 7/2^+$	306.31	5.749	4.42	5.78	1.30	1.01
$7/2^+ \rightarrow 5/2^+$	319.23	5.118	4.42	4.92	1.16	1.04
$7/2^+ \rightarrow 7/2^+$	442.42	6.860	4.42	4.16	1.55	1.65
			^{113}Rh → ^{113}Pd			
$7/2^+ \rightarrow 5/2^+$	0	5.400	4.61	3.61	1.17	1.50
$7/2^+ \rightarrow 7/2^+$	189.51	5.900	4.59	5.24	1.28	1.13
$7/2^+ \rightarrow 5/2^+,7/2^+$	349.15	5.000	5.66	5.25	1.13	1.05
$7/2^+ \rightarrow 5/2^+,7/2^+$	372.99	6.700	5.13	4.59	1.31	1.46
$7/2^+ \rightarrow 5/2^+,7/2^+$	409.24	5.190	4.46	5.64	1.16	1.09
			^{114}Rh → ^{114}Pd			
$1^+ \rightarrow 0^+$	0	5.900	5.33	3.80	1.11	1.55
$1^+ \rightarrow 2^+$	332.61	6.000	5.11	3.79	1.17	1.58
$1^+ \rightarrow 2^+$	694.64	5.700	5.11	5.42	1.12	1.05
$1^+ \rightarrow 0^+$	1115.50	6.100	5.60	4.15	1.09	1.47
$1^+ \rightarrow 2^+$	1391.66	6.100	5.60	4.15	1.09	1.47

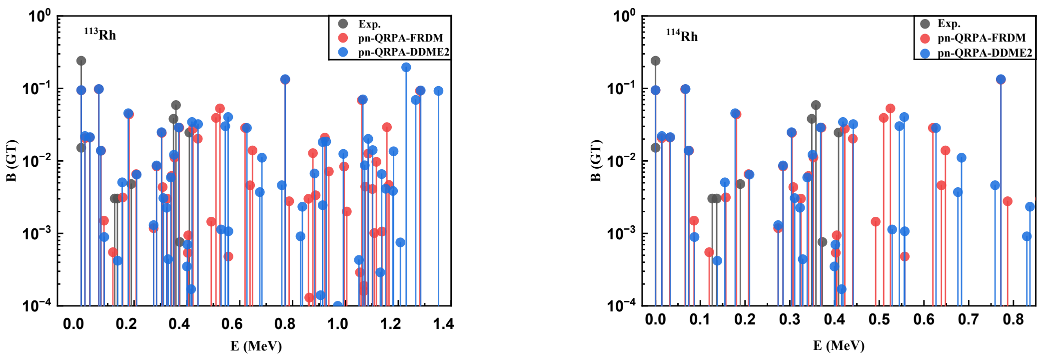

(a) (b)

Figure 3. The GT strength distribution for $^{113-114}$Rh calculated using pn-QRPA-FRDM and pn-QRPA-DDME2-based deformations along with experimental data [34].

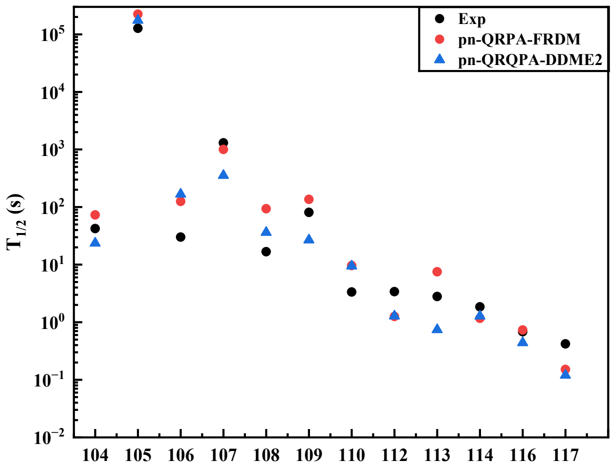

(A)

Figure 4. The present model-based and experimental [33] beta decay half-lives for the Rh nuclei.

on temperature and densities. At finite stellar temperatures, the parent nuclei are thermally populated, and their thermal excitation influences the total weak rates. We analyzed the stellar weak rates at the densities $\rho Y_e = 10^7$, 10^9, and 10^{11} g

Table 3. The sum of $\lambda^{\beta^-}+\lambda^{pc}$ for ^{104,105}Rh isotopes on various densities and temperatures.

ρY_e	T_9	^{104}Rh		^{105}Rh	
		pn-QRPA-FRDM	pn-QRPA-DDME2	pn-QRPA-FRDM	pn-QRPA-DDME2
10^7	3	5.00×10^{-3}	2.68×10^{-8}	4.25×10^{-3}	1.62×10^{-4}
	5	1.14×10^{-2}	1.53×10^{-5}	8.42×10^{-3}	1.79×10^{-3}
	10	1.75×10^{-1}	8.83×10^{-3}	5.33×10^{-2}	1.76×10^{-1}
	25	2.05×10^{2}	1.92×10^{1}	8.98×10^{0}	1.42×10^{2}
	30	8.54×10^{2}	8.88×10^{1}	2.92×10^{2}	5.32×10^{2}
10^9	3	7.33×10^{-8}	7.16×10^{-14}	1.37×10^{-4}	1.65×10^{-9}
	5	2.32×10^{-5}	8.62×10^{-9}	1.15×10^{-1}	6.46×10^{-6}
	10	6.75×10^{-3}	1.59×10^{-4}	5.11×10^{1}	9.56×10^{-3}
	25	6.25×10^{1}	5.83×10^{0}	4.20×10^{2}	4.36×10^{1}
	30	4.04×10^{2}	4.20×10^{1}	1.07×10^{2}	2.53×10^{2}
10^{11}	3	2.62×10^{-39}	6.34×10^{-45}	8.41×10^{23}	3.48×10^{-40}
	5	2.95×10^{-24}	2.43×10^{-27}	1.09×10^{-23}	4.45×10^{-24}
	10	1.94×10^{-12}	7.50×10^{-14}	1.72×10^{-12}	1.03×10^{-11}
	25	4.30×10^{-3}	4.04×10^{-4}	2.20×10^{-4}	3.28×10^{-3}
	30	1.19×10^{-1}	1.23×10^{-2}	4.25×10^{-2}	7.62×10^{-2}

cm^{-3} and at the temperatures T_9 = 3, 5, 10, 25, 30. We have displayed the stellar weak rates for $^{104-116}$Rh in Tables (3-6) using the recipe as mentioned above. Generally, the stellar weak rates decrease with density and increase with temperature. Utilizing both types of interactions, one can see that the stellar rates computed via the deformation taken from the FRDM are many orders of magnitude higher than the rates computed via the deformation taken from the RMF-DDME2-based interactions at low densities and low temperatures. However, at higher temperatures, $T_9 \approx 30$, the rates are enhanced by a factor of 10 or less.

Table 4. The sum of $\lambda^{\beta^-}+\lambda^{pc}$ for ^{106,107,108}Rh isotopes on various densities and temperatures.

ρY_e	T_9	^{106}Rh		^{107}Rh		^{108}Rh	
		pn-QRPA-FRDM	pn-QRPA-DDME2	pn-QRPA-FRDM	pn-QRPA-DDME2	pn-QRPA-FRDM	pn-QRPA-DDME2
10^7	3	1.51×10^{-5}	2.35×10^{-7}	4.25×10^{-2}	7.42×10^{-2}	2.86×10^{-2}	7.42×10^{-2}
	5	7.86×10^{-5}	8.21×10^{-5}	6.10×10^{-2}	1.08×10^{-1}	6.10×10^{-2}	1.08×10^{-1}
	10	1.65×10^{-2}	2.23×10^{-2}	7.91×10^{-1}	7.34×10^{-1}	7.91×10^{-1}	7.34×10^{-1}
	25	5.85×10^{1}	2.68×10^{1}	6.18×10^{2}	2.13×10^{2}	6.18×10^{2}	2.13×10^{2}
	30	2.87×10^{2}	1.19×10^{2}	2.32×10^{3}	7.23×10^{2}	2.32×10^{3}	7.23×10^{2}
10^9	3	1.88×10^{-11}	3.16×10^{-12}	6.44×10^{-7}	2.62×10^{-6}	6.44×10^{-7}	2.62×10^{-6}
	5	4.12×10^{-8}	8.60×10^{-8}	1.11×10^{-4}	4.01×10^{-4}	1.11×10^{-4}	4.01×10^{-4}
	10	1.62×10^{-4}	5.28×10^{-4}	3.42×10^{-2}	5.86×10^{-2}	3.42×10^{-2}	5.86×10^{-2}
	25	1.77×10^{1}	8.17×10^{0}	1.89×10^{2}	6.67×10^{1}	1.89×10^{2}	6.67×10^{1}
	30	1.36×10^{2}	5.64×10^{1}	1.10×10^{3}	3.44×10^{2}	1.10×10^{3}	3.44×10^{2}
10^{11}	3	1.27×10^{-42}	1.50×10^{-43}	1.92×10^{-38}	2.70×10^{-37}	6.17×10^{-1}	3.36×10^{-1}
	5	1.03×10^{-26}	1.39×10^{-26}	1.31×10^{-23}	1.36×10^{-22}	9.75×10^{-1}	4.03×10^{-1}
	10	5.01×10^{-14}	1.80×10^{-13}	1.09×10^{-11}	3.73×10^{-11}	9.92×10^{-2}	1.23×10^{0}
	25	1.21×10^{-3}	5.66×10^{-4}	1.31×10^{-2}	5.10×10^{-3}	9.75×10^{1}	1.05×10^{2}
	30	3.98×10^{-2}	1.66×10^{-2}	3.25×10^{-1}	1.05×10^{-1}	4.24×10^{2}	3.49×10^{2}

Table 5. The sum of $\lambda^{\beta^-}+\lambda^{pc}$ for ^{109,110,112}Rh isotopes on various densities and temperatures.

ρY_e	T_9	^{109}Rh		^{110}Rh		^{112}Rh	
		pn-QRPA-FRDM	pn-QRPA-DDME2	pn-QRPA-FRDM	pn-QRPA-DDME2	pn-QRPA-FRDM	pn-QRPA-DDME2
10^7	3	6.17×10^{-1}	3.36×10^{-1}	4.25×10^{-1}	1.63×10^{0}	5.97×10^{-2}	1.11×10^{1}
	5	9.75×10^{-1}	4.03×10^{-1}	4.76×10^{-1}	2.00×10^{0}	8.27×10^{-2}	1.24×10^{1}
	10	9.92×10^{-2}	1.23×10^{0}	2.11×10^{0}	4.75×10^{0}	2.40×10^{1}	2.40×10^{1}
	25	9.75×10^{1}	1.05×10^{2}	7.77×10^{2}	2.03×10^{2}	2.04×10^{2}	2.19×10^{2}
	30	4.24×10^{2}	3.49×10^{2}	2.74×10^{3}	6.16×10^{2}	5.44×10^{2}	6.05×10^{2}
10^9	3	2.11×10^{-7}	3.67×10^{-4}	1.06×10^{-1}	2.89×10^{-2}	1.53×10^{-9}	1.99×10^{-1}
	5	2.08×10^{-5}	5.30×10^{-3}	2.64×10^{-3}	1.01×10^{-1}	1.79×10^{-3}	3.27×10^{-1}
	10	3.64×10^{-1}	2.00×10^{-1}	1.26×10^{-1}	1.08×10^{0}	2.40×10^{-2}	7.42×10^{0}
	25	2.98×10^{1}	3.53×10^{1}	2.39×10^{2}	7.52×10^{1}	2.04×10^{2}	2.19×10^{2}
	30	2.01×10^{2}	1.69×10^{2}	1.30×10^{3}	3.06×10^{2}	5.44×10^{2}	6.05×10^{2}
10^{11}	3	9.04×10^{-39}	1.47×10^{-34}	4.13×10^{-36}	9.91×10^{-32}	3.44×10^{-40}	7.57×10^{-30}
	5	3.25×10^{-24}	6.41×10^{-21}	3.66×10^{-22}	5.78×10^{-19}	4.50×10^{-24}	1.25×10^{-17}
	10	1.22×10^{-12}	2.85×10^{-10}	3.97×10^{-11}	5.06×10^{-9}	1.12×10^{-11}	4.62×10^{-8}
	25	2.06×10^{-3}	5.81×10^{-2}	1.67×10^{-2}	1.35×10^{-1}	3.41×10^{-3}	4.02×10^{-2}
	30	5.92×10^{-2}	5.81×10^{-2}	3.85×10^{-1}	1.35×10^{-1}	7.84×10^{-2}	2.50×10^{-1}

Table 6. The sum of λ^{β^-}+λ^{pc} for ^{113,114,116}Rh isotopes on various densities and temperatures.

ρY_e	T_9	^{113}Rh		^{114}Rh		^{116}Rh	
		pn-QRPA-FRDM	pn-QRPA-DDME2	pn-QRPA-FRDM	pn-QRPA-DDME2	pn-QRPA-FRDM	pn-QRPA-DDME2
10^7	3	1.28×10^{0}	1.45×10^{0}	2.14×10^{-1}	3.46×10^{0}	1.13×10^{1}	1.71×10^{1}
	5	1.46×10^{0}	1.66×10^{0}	2.83×10^{-1}	3.64×10^{0}	1.29×10^{1}	2.59×10^{1}
	10	4.22×10^{0}	3.73×10^{0}	8.09×10^{-1}	9.56×10^{0}	5.28×10^{1}	5.44×10^{1}
	25	2.56×10^{2}	1.89×10^{2}	3.06×10^{2}	2.19×10^{2}	2.49×10^{2}	3.42×10^{2}
	30	9.12×10^{2}	5.93×10^{2}	1.01×10^{3}	6.01×10^{2}	7.41×10^{2}	8.92×10^{2}
10^9	3	5.48×10^{-2}	2.28×10^{-2}	2.11×10^{-1}	1.57×10^{-1}	1.27×10^{0}	2.99×10^{0}
	5	1.09×10^{-1}	7.55×10^{-2}	3.64×10^{-1}	2.69×10^{-1}	1.29×10^{1}	5.75×10^{0}
	10	7.98×10^{-1}	7.97×10^{-1}	1.95×10^{0}	2.54×10^{0}	1.27×10^{1}	1.81×10^{1}
	25	8.64×10^{1}	6.75×10^{1}	1.09×10^{2}	9.34×10^{1}	2.49×10^{2}	1.46×10^{2}
	30	4.41×10^{2}	2.91×10^{2}	4.93×10^{2}	3.12×10^{2}	7.41×10^{2}	4.60×10^{2}
10^{11}	3	2.40×10^{-32}	2.63×10^{-32}	1.17×10^{-30}	5.87×10^{-30}	1.13×10^{-10}	1.08×10^{-8}
	5	5.64×10^{-20}	1.73×10^{-19}	6.12×10^{-19}	1.00×10^{-17}	6.12×10^{-9}	4.04×10^{-8}
	10	4.75×10^{-10}	2.01×10^{-9}	1.70×10^{-9}	4.04×10^{-8}	1.70×10^{-7}	2.77×10^{-8}
	25	7.69×10^{-3}	9.50×10^{-3}	1.15×10^{-2}	3.73×10^{-2}	1.15×10^{-2}	2.29×10^{-2}
	30	1.41×10^{-1}	1.12×10^{-1}	1.69×10^{-1}	2.36×10^{-1}	1.30×10^{-1}	2.02×10^{-1}

4. CONCLUSIONS

In this work, we performed the analysis for neutron-rich $^{104-116}$Rh isotopes using the RMF and pn-QRPA models. The nuclear shapes and their deformation are computed via the RMF framework, and the β-decay properties, including the GT strength, the decay half-lives, and the log ft values, are analyzed via the pn-QRPA framework. The half-lives and log ft values are obtained using the deformed pn-QRPA model, with β_2 taken from the FRDM and RMF DD-ME2 based interaction, are reasonably consistent with existing experimental data. Additionally, we have calculated the stellar β-decay rates based on the deformed pn-QRPA model. Our analysis demonstrates a strong dependence on both temperature and density. At lower temperatures, the ground-state transitions dominate the stellar weak rates because excited-state populations are lower, whereas excited-state populations increase significantly at higher temperatures, which impacts the stellar weak rates. Increasing the density generally suppresses β-decay rates due to phase-space constraints. Overall, stellar β-decay rates rise with temperature and fall with increasing density.

Declaration of competing interest: The authors declare that they have no known competing financial interests or personal relationships that could have appeared to influence the work reported in this paper.

ORCID

Abdul Kabir, https://orcid.org/0000-0002-9344-975X; **Jameel-Un Nabi**, https://orcid.org/0000-0002-8229-8757; **Rahat Badshah**, https://orcid.org/0009-0001-1900-6301; **Ayesha Anjum**, https://orcid.org/0009-0000-2290-7891

REFERENCES

[1] J.-Un Nabi, A. Kabir, and T. Bayram, Chin. J. Phys. **87**, 797 (2024) https://doi.org/10.1016/j.cjph.2023.12.036

[2] H. Kleis, M. Seidlitz, A. Blazhev, L. Kaya, P. Reiter, K. Arnswald, A. Dewald, *et al*. Phys. Rev. C, **104**, 034310 (2021). https://doi.org/10.1103/PhysRevC.104.034310

[3] J. P. Fernández-García, M. Cubero, L. Acosta, M. Alcorta, M. A. G. Alvarez, M. J. G. Borge, L. Buchmann, *et al*., Phys. Rev. C, **92**, 044608 (2015). https://doi.org/10.1103/PhysRevC.92.044608

[4] N. Paar, D. Vretenar, and P. Ring, Rept. Prog. Phys.**70**, 691 (2007). https://doi.org/10.48550/arXiv.nucl-th/0701081

[5] J. Engel, M. Bender, J. Dobaczewski, W. Nazarewicz, and R. Surman, *et al*., Phys. Rev. C, **60**, 014302 (1999). https://doi.org/10.1103/PhysRevC.60.014302

[6] Z. M. Niu, Y. F. Niu, H. Z. Liang, W. H. Long, and J. Meng, Phys. Rev. C, **95**, 044301 (2017). https://doi.org/10.1103/PhysRevC.95.044301

[7] A. Kabir, J.-Un Nabi, S.A. Rida, I. Anwaar, N.-Ul A. Raza, and H. Almujibah, Res. Astron. Astrophys. **25**, 015004 (2025). https://doi.org/10.1088/1674-4527/ad981d

[8] E. Bouchez, I. Matea, W. Korten, F. Becker, B. Blank3 C. Borcea, A. Buta, *et al*., Phys. Rev. Lett. **90**, 082502 (2003). https://doi.org/10.1103/PhysRevLett.90.082502

[9] M. Rajput, S. Singh, V. Rani, P. Verma, A. Bharti, G. H. Bhat, and J. A. Sheikh, Eur. Phys. J. A, **58**, 146 (2022). https://doi.org/10.1140/epja/s10050-022-00802-x

[10] U. Hager, V.-V. Elomaa, T. Eronen, J. Hakala, A. Jokinen, A. Kankainen, S. Rahaman, *et al*., Phys. Rev. C, **75**, 064302 (2007). https://doi.org/10.1103/PhysRevC.75.064302

[11] M. Hukkanen, W. Ryssens, P. Ascher, M. Bender, T. Eronen, S. Grévy, A. Kankainen, *et al*., Phys. Rev. C, **107**, 014306 (2024). https://doi.org/10.1103/PhysRevC.107.014306

[12] J. F. W. Lane, A. N. Andreyev, S. Antalic, D. Ackermann, J. Gerl, F. P. Heßberger, S. Hofmann, *et al*., Phys. Rev. C, **87**, 014318 (2013). https://doi.org/10.1103/PhysRevC.87.014318

[13] M. Versteegen, D. Denis-Petit, V. Méot, T. Bonnet, M. Comet, F. Gobet, F. Hannachi, *et al*., Phys. Rev. C, **94**, 044325 (2016). https://doi.org/10.1103/PhysRevC.94.044325

[14] J.-U. Nabi, H. V. Klapdor-Kleingrothaus, and H. Volker, At. Data Nucl. Data Tables **88**, 237 (2004). https://doi.org/10.1016/j.adt.2004.09.002

[15] A. Kabir, J.-U. Nabi, and M. Zubair, Eur. Phys. J. A, **141**, 249 (2026). https://doi.org/10.1140/epjp/s13360-026-07376-3

[16] J. D. Walecka, Ann. Phys. **83**, 491 (1974). https://doi.org/10.1016/0003-4916(74)90208-5

[17] P. Ring, Prog. Part. Nucl. Phys. **37**, 193 (1996). https://doi.org/10.1016/0146-6410(96)00054-3

[18] S. Typel, and H. H. Wolter, Nucl. Phys. A **656**, 331 (1999). https://doi.org/10.1016/S0375-9474(99)00310-3

[19] G. A. Lalazissis, T. Nikšić, D. Vretenar, and P. Ring, Phys. Rev. C **71**, 024312 (2005). https://doi.org/10.1103/PhysRevC.71.024312

[20] J. Meng, H. Toki, S.G. Zhou, S.Q. Zhang, W.H. Long, and L.S. Geng, Prog. Part. Nucl. Phys.**57**, 470 (2006). https://doi.org/10.1016/j.ppnp.2005.06.001

[21] T. Nikšić, D. Vretenar, and P. Ring, Phys. Rev. C, **78**, 034318 (2008). https://doi.org/10.1103/PhysRevC.78.034318

[22] J.-U. Nabi, W. Khalid, A. Kabir and S. A. Rida, Arab. J. Sci. Eng. **50**, 6865 (2025). https://doi.org/10.1007/s13369-024-09619-w

[23] T. Nikšić, N. Paar, D. Vretenar, and P. Ring, Comput. Phys. Commun. **185**, 1808 (2014). https://doi.org/10.1016/j.cpc.2014.02.027

[24] S. Karatzikos, A. V. Afanasjev, G. A. Lalazissis, and P. Ring, Phys. Lett. B, **689**, 72 (2010). https://doi.org/10.1016/j.physletb.2010.04.045

[25] B. Mottelson, The Nilsson Model and Sven Gösta Nilsson. Phys. Scr. **T125** (2006). https://doi.org/10.1088/0031-8949/2006/T125/E02

[26] K. Ikeda, S. Fujii, and J. I. Funjita, Phys Lett. **3**, 271 (1963). https://doi.org/10.1016/0031-9163(63)90255-5

[27] J. C. Hardy, and I. S. Towner, Phys. Rev. C, **79**, 055502 (2009). https://doi.org/10.1103/PhysRevC.79.055502

[28] M. Hirsch, A. Staudt, K. Muto, and H. V. Klapdor-Kleingrothaus, Nucl. Phys. A, **535,** 62 (1991). https://doi.org/10.1016/0375-9474(91)90515-8

[29] K. Muto, E. Bender, T. Oda, and H. V. Klapdor-Kleingrothaus, Phys. A - Hadron Nucl. **341**, 407 (1992). https://doi.org/10.1007/BF01301384

[30] N. B. Gove, and M. J. Martin, At. Data Nucl. Data Tables **10**, 205 (1971). https://doi.org/10.1016/S0092-640X(71)80026-8

[31] A. Kabir, J.-U. Nabi, N. U. A. Raza, and H. Almujibah, Nucl. Phys. A, **1057**, 123057 (2025). https://doi.org/10.1016/j.nuclphysa.2025.123057

[32] P. Möller, A.J. Sierk, T. Ichikawa, and H. Sagawa, At. Data Nucl. Data Tables, **109–110**, 1–204. (2016). https://doi.org/10.1016/j.adt.2015.10.002

[33] M. Wang, W. J. Huang, F. G. Kondev, G. Audi, and S. Naimi, Chin. Phys. C, **45**, 030003 (2021). https://doi.org/10.1088/1674-1137/abddaf

[34] National Nuclear Data Center, Brookhaven National Laboratory. ”Nudat (nuclear structure and decay data).” (2008). https://www.nndc.bnl.gov/

[35] S. Usman, and A. Mushtaq Sci. Rep. **13** 15315 (2023). https://doi.org/10.1038/s41598-023-42397-3

СТОСОВНО ЯДЕРНОЇ СТРУКТУРИ ТА СЛАБКУ ШВИДКІСТЬ ЗОРЯНОГО РОЗПАДУ БАГАТОГО НА НЕЙТРОНИ ІЗОТОПУ $^{104-116}$Rh

Абдул Кабір[1], Джаміль-Ун Набі[2], Рахат Бадшах[1], Аєша Анджум[2]

[1]*Кафедра космічних наук, Інститут космічних технологій, Ісламабад, 44000, Пакистан*

[2]*Кафедра фізики, Університет Ваха, Ваканте, 47040, Пакистан*

Основний стан ядра та властивості бета-розпаду багатих на нейтрони непарних-непарних та непарних-A ізотопів родію $^{104-116}$Rh досліджуються за допомогою моделей релятивістського середнього поля (RMF) та наближення випадкової фази протон-нейтронних квазічастинок (pn-QRPA). Розподіл сили Гамова-Теллера (GT) та властивості β-розпаду отримані на основі параметрів деформації основного стану з розрахунків RMF та включені в структуру наближення квазічастинкової випадкової фази. Поверхні потенційної енергії та криві потенційної енергії досліджуються для дослідження ядерної стабільності та переходів форми. Розраховані періоди напіврозпаду та значення $\log ft$ добре узгоджуються з існуючими експериментальними даними, що підтверджує використання ядерних моделей. Крім того, швидкості слабкої взаємодії зі зорями розраховані як функція щільності та температури, що підкреслює їх вплив на нуклеосинтез в астрофізичних середовищах. Для нейтроно-багатих ізотопів Rh результати надають корисні дані про структуру ядра та надійні вхідні дані для моделювання r-процесу.

Ключові слова: *pn-QRPA; властивості основного стану ядра; ядерні деформації; поверхні потенційної енергії; log ft*